remote sensing

MDPI

Article

Monitoring Irrigation Events and Crop Dynamics Using Sentinel-1 and Sentinel-2 Time Series

Chunfeng Ma [1,2,*], Kasper Johansen [1] and Matthew F. McCabe [1]

[1] Hydrology, Agriculture and Land Observation Group, Water Desalination and Reuse Center, Division of Biological and Environmental Sciences and Engineering, King Abdullah University of Science and Technology (KAUST), Thuwal 23955-6900, Saudi Arabia; kasper.johansen@kaust.edu.sa (K.J.); matthew.mccabe@kaust.edu.sa (M.F.M.)

[2] Key Laboratory of Remote Sensing of Gansu Province, Northwest Institute of Eco-Environment and Resources, Heihe Remote Sensing Experimental Research Station of Chinese Academy of Sciences, Lanzhou 730000, China

* Correspondence: chunfeng.ma@kaust.edu.sa or machf@lzb.ac.cn

Abstract: Capturing and identifying field-based agricultural activities, such as the start, duration and end of irrigation, together with crop sowing/germination, growing period and time of harvest, offer informative metrics that can assist in precision agricultural activities in addition to broader water and food security monitoring efforts. While optically based band-ratios, such as the normalized difference vegetation index (NDVI) and normalized difference water index (NDWI), have been used as descriptors for monitoring crop dynamics, data are not always available due to the influence of clouds and other atmospheric effects on optical sensors. Satellite-based microwave systems, such as the synthetic aperture radar (SAR), offer an all-weather advantage in monitoring soil and crop conditions. In this paper, we leverage the relative strengths of both optical- and microwave-based approaches by combining high resolution Sentinel-1 SAR and Sentinel-2 optical imagery to monitor irrigation events and crop dynamics in a dryland agricultural landscape. A microwave backscatter model was used to analyze the responses of simulated backscatters to soil moisture, NDVI and NDWI (both are correlated with vegetation water content and can be regarded as vegetation descriptors), allowing an empirical relationship between these two platforms. A correlation analysis was also performed using Sentinel-1 SAR and Sentinel-2 optical data over crops of maize, alfalfa, carrot and Rhodes grass in Al Kharj farm of Saudi Arabia to identify an appropriate SAR-based vegetation descriptor. The results illustrate the relationship between SAR and both NDVI and NDWI and demonstrated the relationship between the cross-polarization ratio (VH/VV) and the two optical indices. We explore the capacity of this multi-platform and multi-sensor approach to inform on the spatio-temporal dynamics of a range of agricultural activities, which can be used to facilitate field-based management decisions.

Keywords: synthetic aperture radar; normalized difference vegetation index; normalized difference water index; Sentinel-1; Sentinel-2; irrigation; crop dynamics

Citation: Ma, C.; Johansen, K.; McCabe, M.F. Monitoring Irrigation Events and Crop Dynamics Using Sentinel-1 and Sentinel-2 Time Series. *Remote Sens.* **2022**, *14*, 1205. https://doi.org/ 10.3390/rs14051205

Academic Editors: Guido D'Urso, Onur Yüzügüllü and Kyle Knipper

Received: 9 January 2022
Accepted: 6 February 2022
Published: 1 March 2022

1. Introduction

Climate change and population growth have driven an increasing demand for irrigation water to support agricultural production, making this one of the most serious issues facing arid and semi-arid regions around the world [1,2]. As such, quantifying water use for agriculture and monitoring crop status represent critical sources of information for optimizing water allocation and improving agricultural productivity [3,4]. It is also important to develop the capacity to monitor and characterize field-scale events, including activities, such as irrigation scheduling (e.g., start, duration and end of irrigation) and related crop dynamics, capturing activities including the sowing date, growing period and time of harvest. In many cases, these activities can be identified through time series

characteristics of the normalized difference vegetation index (NDVI) [5–8] and normalized difference water index (NDWI), facilitating the retrieval of information not just to improve agricultural water use management, but also to provide further insight into the security of our food and water systems.

Satellite remote sensing in the optical and shortwave infrared bands has long been an effective approach for monitoring crop dynamics, e.g., the application of vegetation and water indices constructed from multi-spectral band-ratios, such as the NDVI [5–8] and NDWI [9,10]. For example, the moderate-resolution imaging spectroradiometer (MODIS) derived enhanced vegetation index has previously been used to determine crop phenological features (including planting/germination date, heading date and harvesting/maturity date) [11]. Similarly, the fusion of multi-platform/sensor data have been widely applied in crop phenology tracking [12,13] and crop intensity mapping [14]. However, optical sensors are limited to cloud-free conditions. On the other hand, synthetic aperture radar (SAR) sensors can overcome this limitation due to their cloud-penetrating capabilities [15,16]. The SAR signal can also penetrate the crop canopy and sense the information from both the vegetation and soil surface, providing a more comprehensive understanding of crop and soil moisture conditions. Relative to visible and thermal remote sensing, SAR data have only been applied to a limited extent for agricultural monitoring, partly because of the uncertainties in backscattering models [17] and the inherent speckle noise of SAR images [18].

Capturing irrigation events and monitoring crop dynamics at agricultural field scales require a high spatiotemporal resolution remote sensing time series. With recent developments in Earth observation platforms, including through the availability of CubeSat [19] and Sentinel constellations [20], high spatiotemporal resolution imagery have become increasingly available. The Sentinel missions of the European Space Agency (ESA) provide an unprecedented opportunity for agriculture monitoring, as they deliver radiometrically calibrated high spatial resolution imagery (10 m) with up to 5 days revisit time. Sentinel-1 [21–23] includes a C-band SAR, while Sentinel-2 [24,25] offers a multispectral instrument that measures the Earth's reflected radiance across 13 spectral bands located in the visible, near infrared and shortwave infrared.

The combined use of high spatio-temporal resolution data acquired from both the SAR and optical Sentinel platforms provides enhanced sensing capabilities to monitor the status and processes of agricultural fields, including for soil moisture retrieval [21,22,26–29], crop classification and mapping [30,31], vegetation phenology monitoring [32,33] and many other applications. Although several studies have explored the combination of Sentinel-1 SAR and Sentinel-2 optical images for crop type mapping [34–36], how to establish a connection between the optical and SAR signals to develop an integrated analysis of agricultural dynamics has not been reported. For example, Veloso et al. [37] analyzed the temporal backscattering and NDVI behavior of various crops using time series of Sentinel-1 and Sentinel-2-like data (including SPOT5-Take5, Landsat-8, Deimos-1 and Formosat-2). They demonstrated that the dense time series of Sentinel data allowed for an assessment of short phenological stages. However, they did not analyze in detail how to link the optical and SAR signals for the integrated analysis of crop dynamics.

The relative strength of combining optical and SAR data from two platforms may lead to a more comprehensive monitoring of irrigation and crop dynamics than the use of any single platform. While optical data can provide information on crop extent, condition and the temporal span of growing seasons, SAR data are well suited for measuring soil moisture and vegetation water content. Thus, establishing relationships between SAR and optical data is key to enhance monitoring capabilities of agricultural field processes. To generalize results to a range of agricultural systems, modeling the relationship between SAR backscatter and optically derived NDVI and NDWI prior to jointly monitoring crops and irrigation with Sentinel-1 and Sentinel-2 time series is necessary. An investigation of the combined use of SAR backscatters and NDVI has been reported [38,39]. These studies utilized regression to explore statistical relationships between NDVI and backscatters or

interferometric coherence, but did not seek to interpret the physical principles behind the backscattering process. The backscattering modeling presented herein aims to explore the backscattering mechanism, providing an improved and more generalized understanding of the SAR time series.

The overall aim of this paper was to identify a number of important irrigation activities (i.e., start, duration and end of irrigation) and crop dynamics (including sowing, growing and harvest dates), by combining Sentinel-1 and Sentinel-2 observations. To do this, relationships between SAR signals and soil moisture, NDVI and NDWI were examined using a backscattering model combined with an estimation scheme for vegetation water content (VWC). A correlation analysis between SAR and both NDVI and NDWI was then undertaken for a range of different crop types, including maize, alfalfa, carrot and Rhodes grass, as well as for bare soil. These analyses provided a foundation for interrogating the remote sensing time series data under different crop and irrigation conditions, with key irrigation events and crop status identified accordingly.

2. Site Description and Data

2.1. Study Area

Saudi Arabia is a water scarce country with annual rainfall rarely exceeding 100 mm in most places [40]. Since the mid-1980s, the Kingdom has witnessed a rapid development and expansion in agriculture [2]. While this development successfully increased the country's production of a number of key crops, the hot and dry climate and scarce water resources make it extremely difficult to develop agriculture in a sustainable manner. The present study focuses on an irrigated agricultural area in the Al Kharj region, approximately 200 km southeast of Riyadh (Figure 1). The site consists of 47 center pivot fields with a total area of approximately 2400 ha [41,42]. The terrain is relatively flat, with an average elevation of 380 m. The farm was predominantly planted with maize, alfalfa, carrot and Rhodes grass. All fields are irrigated using center pivot systems.

The study spans the time period from January 2016 to December 2018, during which time some fields were planted with the same crop type, while other fields had alternating crop types. For example, pivot P22 (see Figure 1) was cultivated with alfalfa from January 2016 to November 2017, while TE-10 was cultivated with alfalfa from January to July 2016 and maize from August 2016 to the end of 2017.

2.2. Remote Sensing Data and Preprocessing

The pair of satellites that comprise Sentinel-1 (A and B) carry C-band SAR sensors, while the Sentinel-2 pair (A and B) carry multispectral imaging optical sensors. Both platforms can provide images with a spatial resolution of up to 10 m. Detailed descriptions of the satellites and their imagery can be found in [24,29,43]. Sentinel-1 data were collected in the interferometric width (IW) mode with dual-polarizations (VV and VH) at a spatial resolution of 10 m. To ensure backscatter consistency, only images with an ascending orbit and an incidence angle of approximately 310 were used, providing a time series of 77 Sentinel-1A data acquired from 21 February 2016 to 19 December 2018, generally with a 12-day interval between images. Sentinel-1B images were not used because limited images were available over the region during the study period. The collected images were Level-1 products that have been multi-looked and projected to ground-range [27]. The collected images were preprocessed by Google Earth Engine (GEE) [44] using the Sentinel-1 Toolbox [45] for thermal noise removal, radiometric calibration and terrain correction. To reduce the inherent speckle noise of the SAR images, speckle filtering was carried out using a 3×3 boxcar filter on the GEE platform before downloading the data [46].

A total of 108 Level 1C Sentinel-2A and Sentinel-2B images acquired between 9 January 2016 and 14 December 2018 were downloaded from the ESA database at (https://scihub.copernicus.eu (accessed on 9 January 2019)) providing an average interval of 10 days. The images were geometrically orthorectified and corrected to top-of-atmosphere reflectance. To produce at-surface reflectance values, an atmospheric correction of the

imagery was conducted using the sen2cor procedure [47], which is an extension plugin for the ESA Sentinel Application Platform [45]. The Sentinel-2 image bands have three different spatial resolutions: Bands 2 (496 nm), 3 (560 nm), 4 (665 nm) and 8 (833 nm) have 10 m pixels, whereas bands 5 (704 nm), 6 (740 nm), 7 (782 nm), 8A (865 nm), 11 (1614 nm) and 12 (2202 nm) have a spatial resolution of 20 m. The remaining three bands (with 60 m resolution) were not used in our analysis. To match the spatial scale of Sentinel-1, those bands with 20 m resolution were resampled to 10 m using a nearest neighbor resampling technique. Subsequently, NDVI and NDWI were calculated using bands 4, 8A, and 11 of Sentinel-2, respectively (Equations (1) and (2)). Although band 8 has a higher spatial resolution than band 8A, band 8A was used to calculate NDVI and NDWI based on previous analyses that indicated it improved the estimation of soil moisture when using the water cloud model framework (see Ma et al. [29]. These indices were selected for the assessment of vegetation dynamics due to their well-established association with vegetation pigment, phenology and wetness [10,48].

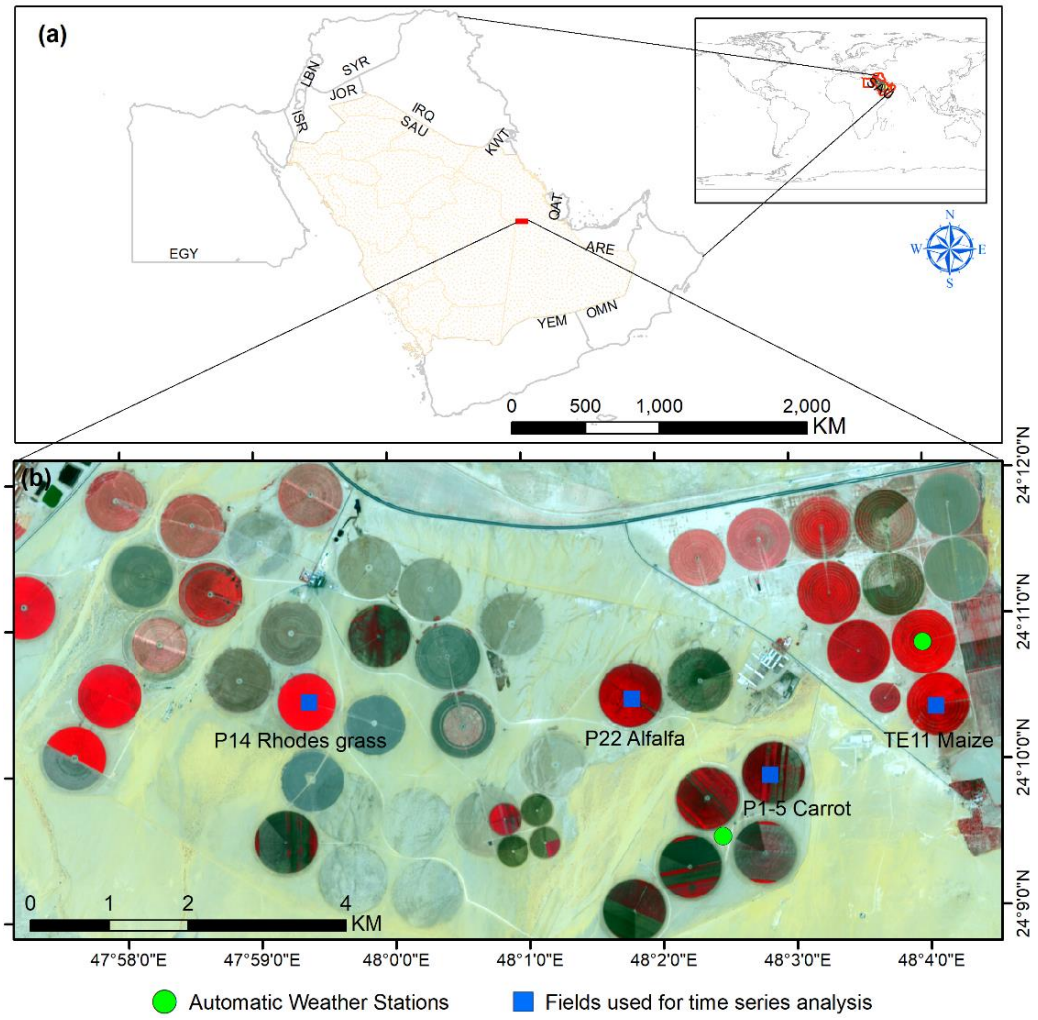

Figure 1. (**a**) The location of the study area in Al Kharj, Saudi Arabia and (**b**) a false color composite Sentinel-2 image from 2 July 2017. The two automatic weather stations (AWS, green circles) for collection of soil moisture and precipitation measurements were located inside a planted center pivot field (namely TE-10 north of TE11) and on bare ground between three fields. The blue squares denote the fields that were used for time series analysis.

$$\mathrm{NDVI} = (\rho_{8A} - \rho_4)/(\rho_{8A} + \rho_4) \quad (1)$$

$$\mathrm{NDWI} = (\rho_{8A} - \rho_{11})/(\rho_{8A} + \rho_{11}) \quad (2)$$

where ρ_i denotes the processed reflectance at ith band.

2.3. Ground Soil Moisture and Farming Records

Soil moisture from HydraProbes (Stevens Water Monitoring Systems, Inc., Portland, OR, USA) installed at 5 cm depth was collected from two site-based weather stations (Figure 1b) for the assessment of soil wetness variation. These data would be used to assess the capacity of the Sentinel-1 and Sentinel-2 time series data to characterize the agronomic processes. One station was located inside an irrigated center pivot field, while the other was located approximately 120 m from a center pivot field on non-irrigated bare ground. Irrigation (monthly irrigation hours and total water applied), sowing and harvesting records were also obtained from farmer-provided records to interpret the key crop growth stages and agronomic events.

3. Methodology

3.1. Theoretical Analysis by Modeling Backscatter

To understand and interpret the time series characteristics of the SAR data over the studied field conditions (e.g., bare soil and vegetated), we first conducted a theoretical analysis using a backscattering model. Specifically, we simulated the VV- and VH-polarized backscatters at the Sentinel-1 C-band frequency and incidence angle configuration using a water cloud model [49,50] to demonstrate the relative contribution of the wetness of soil and vegetation to the microwave backscatter signal.

The water cloud model, which considers the vegetation canopy as cloud-containing water droplets, was proposed to simulate the backscattering from the vegetation canopy and soil surface [49,50]. The model (Equation (3)) has been widely used in vegetated surface modeling and for retrieving parameters, such as soil moisture, due to its simplicity [29]. It simulates the total backscattering signal ($\sigma^0_{total,pq}$) at a linear scale as the contributions of vegetation ($\sigma^0_{veg,pq}$) and soil ($\sigma^0_{soil,pq}$).

$$\sigma^0_{total,pq} = \sigma^0_{veg,pq} + \tau^2 \times \sigma^0_{soil,pq} \tag{3}$$

where $\sigma^0_{soil,pq}$ represents backscatters from the soil surface, which can be modeled by the Oh model [51], a relatively simple (i.e., only one surface roughness parameter is used) approach that has shown similar performance to physical models (such as the integral equation model [52]). In addition, the Oh model can better represent the cross-polarized backscatter compared to physical models and is well suited to the configuration of dual-polarized Sentinel-1 data. τ^2 is the two-way transmissivity that depicts the proportion of backscatters that pass the vegetation canopy twice and are scattered by the soil surface. $\sigma^0_{veg,pq}$ is the vegetation canopy backscattering component. τ^2 and $\sigma^0_{veg,pq}$ are formulated by Equations (4) and (5), respectively.

$$\sigma^0_{veg,pq} = A \times m_V \times cos(\theta) \times \left(1 - \tau^2\right) \times \left(1 - e^{-\alpha}\right) \tag{4}$$

$$\tau^2 = \mathrm{e}^{-2 \times B \times m_V / cos(\theta)} \tag{5}$$

where A, B and α are empirical parameters in the water cloud model, θ is the incidence angle and m_V is vegetation water content that is estimated by NDVI or NDWI using the equations recommended in Gao et al. [6].

$$m_V = 0.098 e^{4.225 \times NDVI} \tag{6}$$

or

$$m_V = 7.84 \times NDWI + 0.6 \tag{7}$$

By doing this, the $\sigma^0_{total,pq}$ can be related to NDVI, NDWI and soil moisture.

In the simulation experiment, the frequency and incidence angle were specified as 5.4 GHz and 31° according to the configuration of the selected Sentinel-1 data. The roughness, specified here as the root mean square height (RMSH), was set to be 1.5 cm. As RMSH was not measured within the study site, the value of 1.5 cm was set according to related measurements over agricultural fields [53]. The empirical parameters A, B and α of the water cloud model were specified as 0.0012, 0.091 and 2.12 for "all land uses" according to Bindlish and Barros [50]. A recently published analysis [29] demonstrated that these parameter values served as the optimal values for a surface with different crops.

3.2. Correlation between Observed Backscatters and Soil Moisture

In addition to forward modeling, the response of real (observed) SAR backscatters was assessed against field-based soil moisture measurements to establish the feasibility of monitoring soil moisture variations based on SAR images. In this experiment, the ground soil moisture was measured at the two field-based climate stations and compared with the corresponding SAR backscatters. To identify irrigation events based on SAR observations, the response of observed SAR backscatters to the measured soil moisture was assessed using linear regression.

3.3. Correlation between Backscatters and NDVI and NDWI

Optical data, such as Sentinel-2 imagery, are affected by cloud cover, whereas SAR data can be obtained irrespective of atmospheric conditions. Hence, SAR data may act as a gap-filler for optical data affected by clouds. NDVI and NDWI derived from Sentinel-2 data were correlated with SAR observations for the four different crop types to determine whether the SAR data were suited for monitoring vegetation conditions. To exploit the potential of VV- and VH-polarized backscatters of Sentinel-1, in addition to the ratio of VH- against VV-polarized backscatters (VH/VV), and to depict vegetation properties (e.g., VWC), we conducted an analysis to observe the correlation of VV-, VH-backscatters and VH/VV against NDVI and NDWI. As both NDVI and NDWI have previously been demonstrated to be correlated to VWC [6,9,10], if high correlations could be found between SAR backscatters (and the ratio of VH/VV) and NDVI (and NDWI), the SAR backscatters and/or VH/VV ratio may also be used to represent VWC. Thus, this correlation analysis aims to test the possibility of replacing NDVI or NDWI with SAR backscatters (or other corresponding indices) to estimate VWC.

3.4. SAR, NDVI and NDWI Time Series of Different Crops

While some center-pivot fields had just a single crop type between January 2016 and December 2018, others had alternating crop types, so the time series behavior of SAR backscatters and NDVI and NDWI will certainly differ. To test this assumption, we compared the SAR backscatters and both NDVI and NDWI for the different crop types. Specifically, the SAR backscatters and NDVI and NDWI from four selected fields (P1-5, P14, P22 and TE11; see Figure 1) that were planted with only a single crop type throughout the study period were first identified. Considering the diameter of each center pivot field was approximately 800 m, a square of 500 $\times$ 500 m inside each field was selected to preclude the sampling of edge pixels along the field perimeter. The retrieved SAR backscatters and the NDVI and NDWI of approximately 2500 pixels were averaged in order to provide a mean value for each field. Based on the identified pixels, differences in NDVI, NDWI and SAR time series among different crops were related to crop types.

To establish differences in time series behavior amongst the crop types, statistics including maximum values (Max), minimum values (Min), amplitude variation (Amp) and standard deviation (Std) were calculated from the time series of NDVI, NDWI and backscatters for the four crops. These were applied to differentiate between the different cover types.

4. Results

4.1. Simulated Responses of Backscatters to Soil Moisture, NDVI and NDWI

A simulation experiment was conducted to test the response of backscatters to soil moisture, NDVI and NDWI based on the water cloud model. Figure 2 shows the responses of the simulated $\sigma^0_{total,pq}$ to soil moisture, while Figure 3 shows the same variable's response to NDVI and NDWI. Both VV- and VH-polarized backscatters increased with increasing soil moisture (Figure 2a,b). At low NDVI and NDWI values, the increasing rate in backscatters was slightly larger than that for high optical index values, e.g., when NDVI is approaching 1.0, the increase in VH-polarized backscatter is minimal. This demonstrates that the backscatters are no longer sensitive to soil moisture at high NDVI and NDWI values.

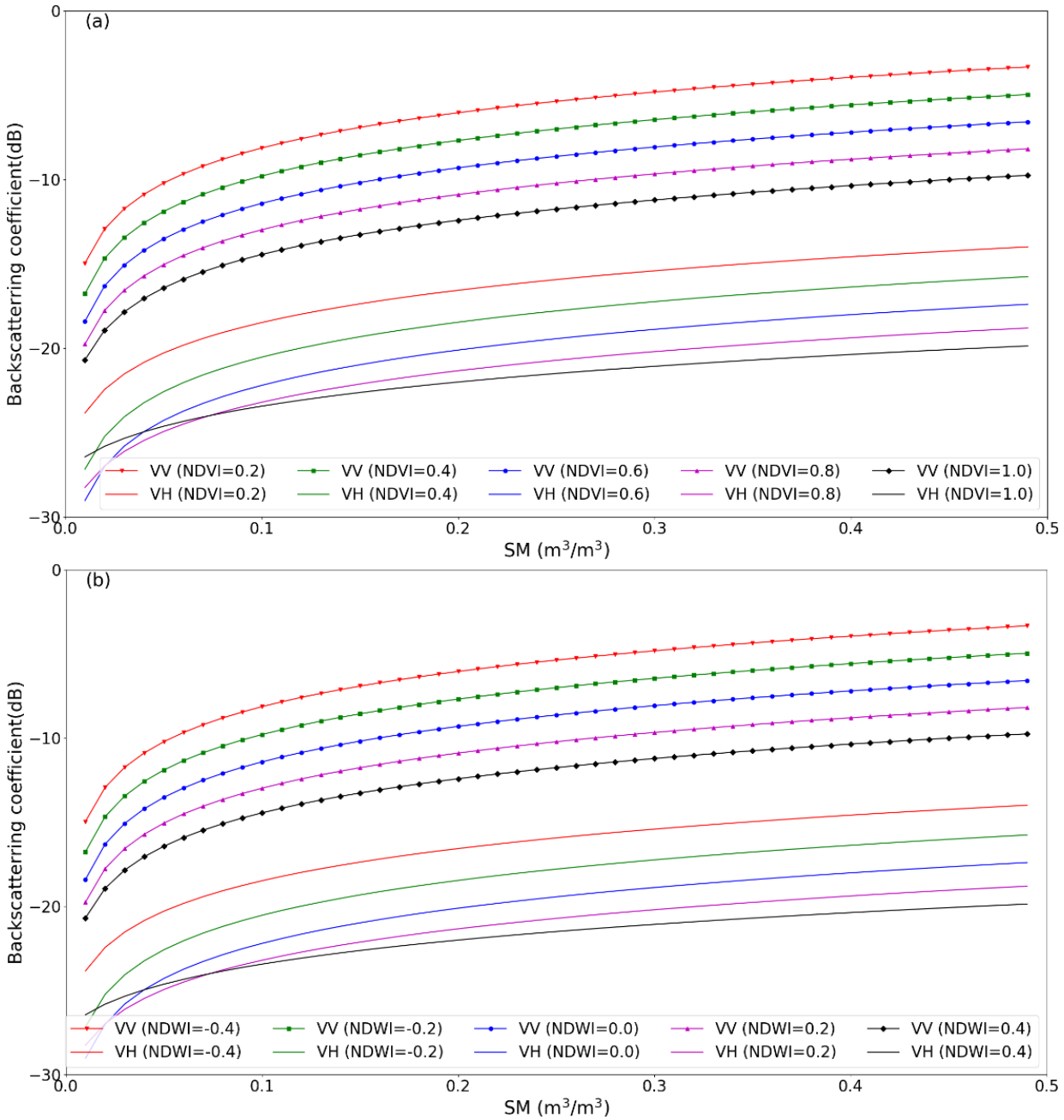

Figure 2. Response of backscatter to soil moisture (SM) at various NDVI (**a**) and NDWI (**b**) levels based on the water cloud model simulations.

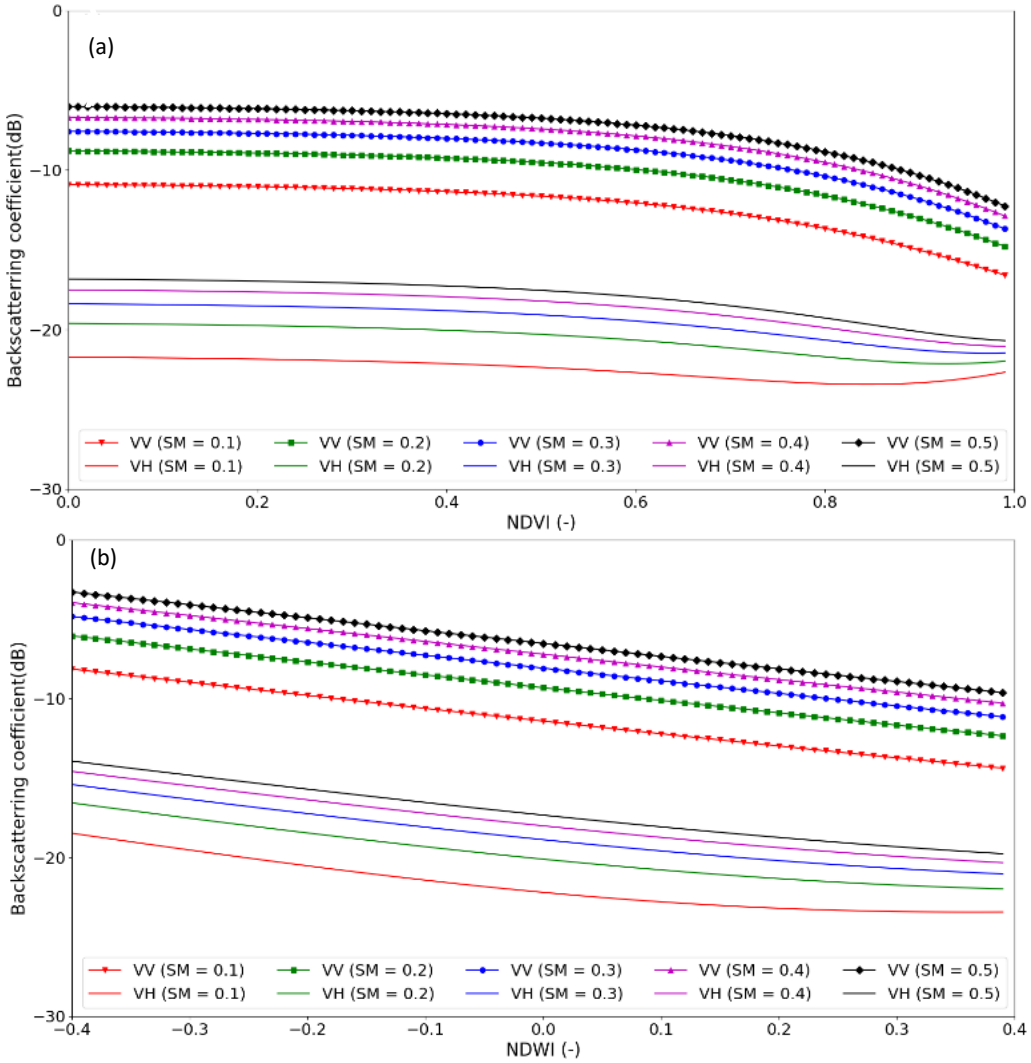

Figure 3. Response of backscatter to NDVI (**a**) and NDWI (**b**) under different soil moisture (SM) levels based on the water cloud model simulations.

Compared to the response of backscatters to the variation of soil moisture, both NDVI and NDWI have much smaller effects on backscatters. As shown in Figure 3a, almost no changes were observed to the backscatters for NDVI up to 0.6, beyond which the VV-polarized backscatter starts decreasing. The VH-polarized backscatter first decreased slightly at NDVI values > 0.60 and then leveled between 0.9–1.0 for soil moisture values > 0.3, or slightly increased for soil moisture values < 0.3. With increasing NDWI, the backscatters demonstrated a relatively minor but consistent decrease (Figure 3b). Comparatively, both VV- and VH-polarized backscatters demonstrated higher sensitivity to soil moisture than to NDVI and NDWI. It should be noted that while these responses varied somewhat with crop type, model parameters (e.g., A, B and α) and radar configurations (frequency and incidence angle), the general trends did not change.

4.2. Evolutions of Observed Soil Moisture Backscatters

Whereas Section 4.1 analyzed the relationships between backscatters and soil moisture based on model simulations, here we evaluate their relationship based on real data to test the feasibility of identifying irrigation events using Sentinel-1. As can be observed from Figure 4, soil moisture was (naturally) much higher in the irrigated center pivot field at TE-10_AWS (Figure 4a) compared with the adjacent bare ground at Desert_AWS (Figure 4b). For the center pivot field, soil moisture was high due to the irrigation applied, whereas

the backscatters showed large changes throughout the time series. Before July 2017, the soil moisture changed with very high frequency, followed by a steady decline. Alfalfa was cultivated and cut frequently during January to July 2016, with an irrigation of 161, 259, 567, 457, 727, 681, and 726 hours according to farmer records for the months from January to July, respectively. From August to November 2016, the field was cultivated with maize and irrigation kept the soil moisture high. After maize harvesting in December 2016, the irrigation ceased until February 2017. During that period, soil moisture dropped sharply, as did backscatters, especially the VH-polarized values. An increase in soil moisture of 0.1 m^3/m^3 was identified for the Desert_AWS in the middle of February 2017, with the cause identified by an 18 mm precipitation event that occurred during 11–15 February 2017. The precipitation event was captured by the SAR image on 15 February with an obvious increase in both VV- and VH-polarized backscatters.

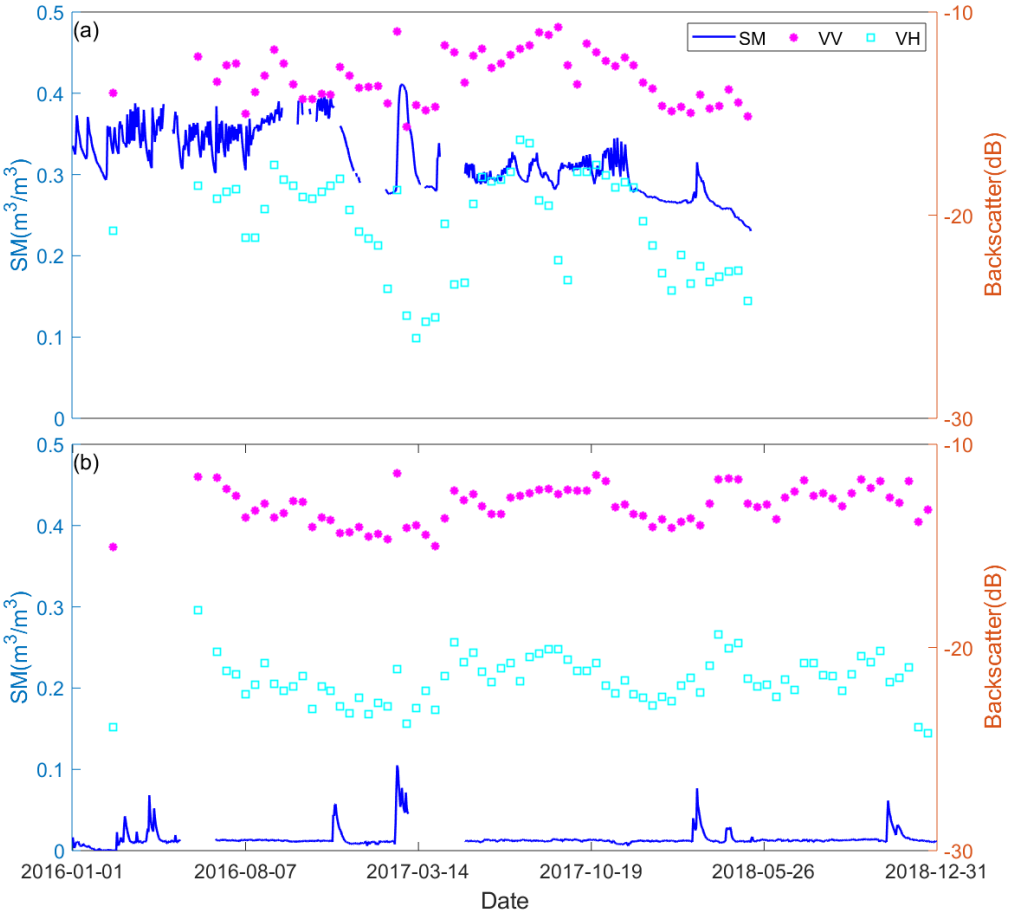

Figure 4. (**a**) The temporal variation of soil moisture (SM) and backscatters at the irrigated field of TE-10_AWS and (**b**) bare ground of Desert_AWS.

Overall, the observed backscatters indicate variations in soil moisture, potentially enabling the identification of irrigation events. The VH-polarized backscatter time series demonstrated larger amplitude than VV-polarized backscatter because the VH-polarized backscatter is influenced more by vegetation than by soil moisture [29,37]. Thus, it is anticipated that the VV-polarized backscatter is better suited for monitoring soil moisture and irrigation [29].

4.3. Correlations between Observed Backscatters and NDVI and NDWI

Considering NDVI and NDWI as basic descriptors of VWC, we analyzed the correlations between SAR backscatters and NDVI and NDWI, aiming to find an optimal SAR-based vegetation descriptor. As shown in Figure 5, the VH/VV ratio produced the

highest correlation with both NDVI (Slope = 0.348, R^2 = 0.531) and NDWI (Slope = 0.423, R^2 = 0.508), respectively, followed by the VH-polarized backscatter. The VH-polarized backscatter demonstrated the highest slope of a linear fitting (Slope = 0.525 for NDVI and Slope = 0.633 for NDWI). Note that the slope here is a normalized slope, i.e., Slope= a/30 where a is the coefficient of the linear model, y = a × x + b. The normalization of the slope was to facilitate the comparison of NDVI and NDWI. The VV-polarized backscatter demonstrated a low correlation and slope with both NDVI (R^2 = 0.210) and NDWI (R^2 = 0.111), consistent with findings in Veloso, et al. [37]. As the NDVI and NDWI were found to estimate VWC [6] and the VH/VV ratio and VH-polarized backscatter were positively correlated to NDVI and NDWI, the VH/VV ratio and VH-polarized backscatter may potentially be used as an alternative for VWC estimation when NDVI and NDWI are unavailable (i.e., under poor weather conditions).

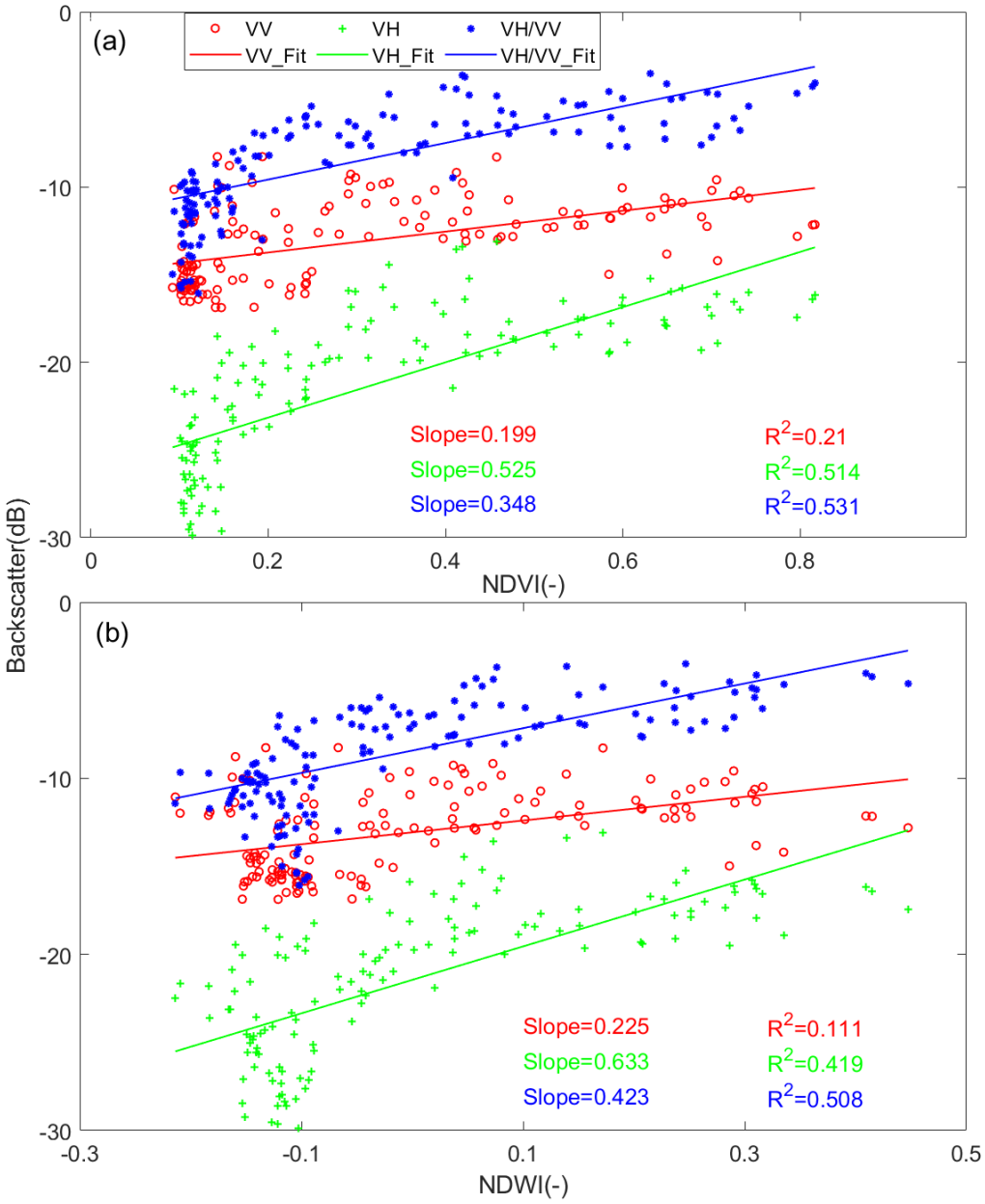

Figure 5. Correlation analysis between SAR backscatters (VV, VH and their ratio VH/VV) and NDVI and NDWI. (**a**) The correlations between backscatters and NDVI, and (**b**) the correlations between backscatter and NDWI. The slope (normalized slope = a/30 where a is the coefficient of linear model y = a × x + b) and R2 were determined based on a linear model.

Of some interest was the sharp increase in SAR backscatter observed for small values of both NDVI and NDWI: an outcome that differed from the model simulation. When investigating the Sentinel-2 imagery and field data, it was verified that for NDVI < 0.15 and NDWI < 0, the fields were mapped as bare surfaces. In such conditions, the variation in backscatter was mainly affected by variations in soil roughness and moisture. With NDVI increasing from 0.15 to 0.5 and NDWI increasing from 0.0 to 0.3, the backscatter is jointly governed by soil moisture, RMSH and VWC. When NDVI and NDWI reached relatively high values, the SAR observations demonstrated a slight decreasing trend. This observation is consistent with the model simulation in Section 4.1.

4.4. Time Series of Remote Sensing Observations

Based on the forward modeling and correlation analysis, we analyzed the time series of NDVI, NDWI and backscatters of the different crops and bare soil with the support of field-based irrigation and farming records. Figures 6–9 show the time series of NDVI, NDWI, backscatters and the ratio of VH/VV for different crops and bare soil. Throughout the time series over the bare soil, NDVI remained stable and low, with a mean value of 0.09, while corresponding NDWI values ranged from −0.2 to 0.04 with a mean value of −0.13. Thus, NDVI and NDWI values < 0.09 and 0, respectively, can be regarded as non-vegetated. Based on these observations, we can identify the specific growing seasons.

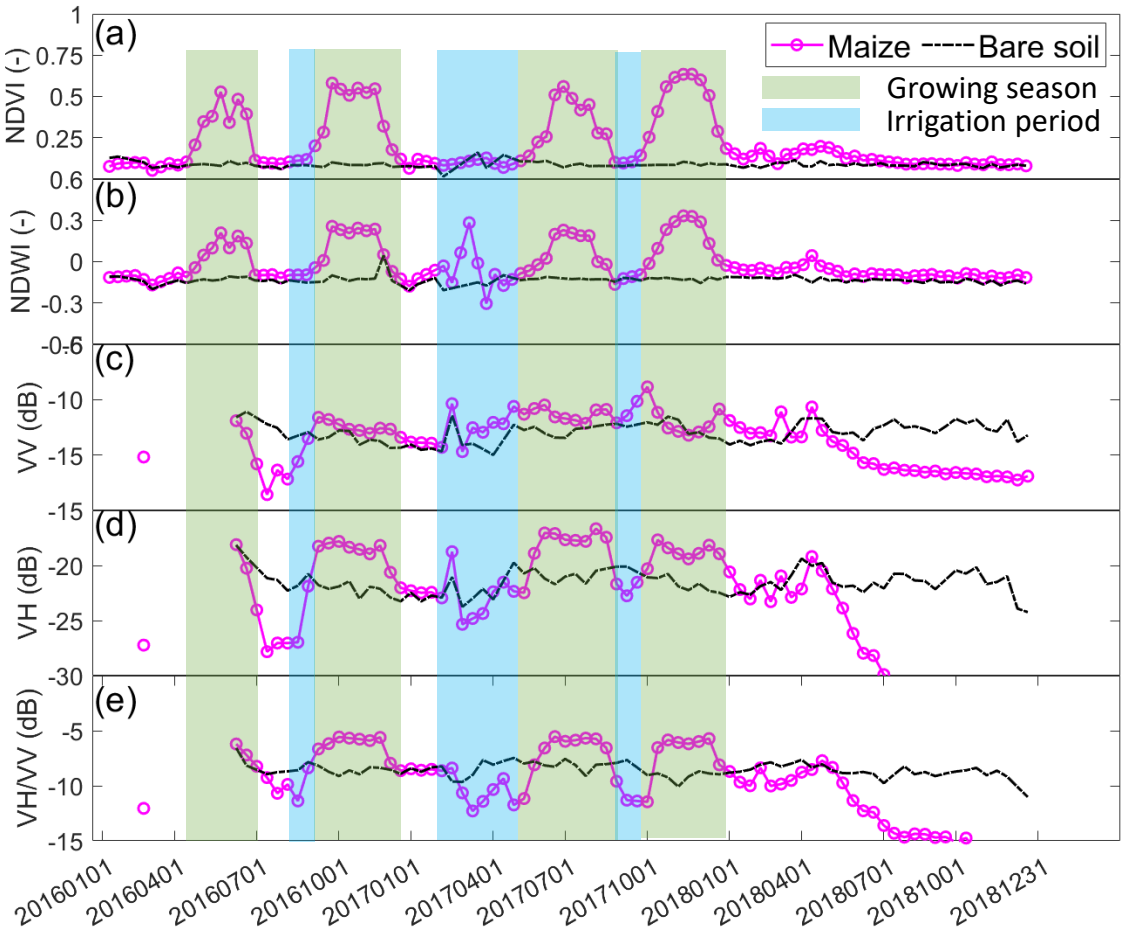

Figure 6. Time series of NDVI (**a**), NDWI (**b**) and backscatters (VV (**c**), VH (**d**) and VH/VV (**e**)) for maize and bare soil from January 2016 to December 2018. The blue bars indicate the beginning of field irrigation in preparation for planting and the green bars indicate the growing seasons of maize, during which the irrigation was applied consistently until the end of the growing season, as per the data collected from the farming records.

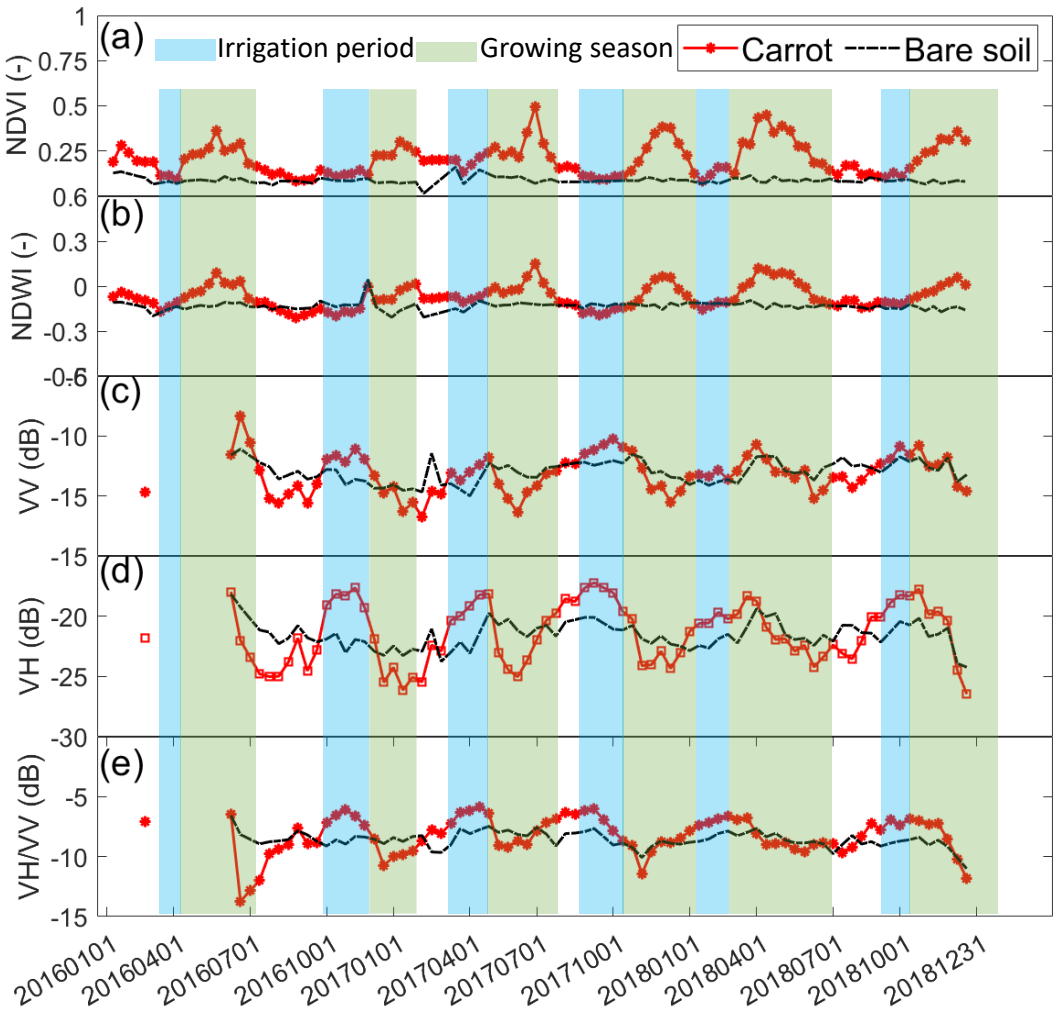

Figure 7. Time series of NDVI (**a**), NDWI (**b**) and backscatters (VV (**c**), VH (**d**) and VH/VV (**e**)) for carrot and bare soil from January 2016 to December 2018. The blue bars indicate the beginning of field irrigation in preparation for planting and the green bars indicate the growing seasons of carrot (where the irrigation was applied consistently throughout the growing season).

From January 2016 to December 2017, there were four maize growing seasons with two seasons per year (Figure 6a,b). In 2016, the first season began in March and ended in June, and the second season ranged from late August to December. However, in 2017, the first season started in May and ended in July, and the second season ran from the end of August until the end of the year. After 2017, the planting of maize ceased in the field and the surface was bare until September 2018. Both time series of NDVI and NDWI clearly present the fluctuations in vegetation, with peaks up to 0.5 and 0.25 for NDVI and NDWI, respectively, occurring during growing seasons. High values with a maximum NDVI of 0.2 and NDWI of 0.0 were observed in May 2018, which may have been caused by the presence of weeds.

The Sentinel-1 backscatters demonstrate seasonal variation over the maize field (Figure 6c–e). Due to limited image availability in the first half of 2016, the time series analysis of Sentinel-1 started from the second growing season (August to December) in 2016. It can be observed that VV- and VH-polarized backscatters started to increase prior to the beginning of each growing season. The starting points occurred around 30 days (or more) and 15–20 days prior to the point where NDVI started to increase for the first (May 2017) and second (September 2017) growing seasons, respectively. From the unirrigated stage to the irrigated stage, VV- and VH-polarized backscatters and their ratio presented a

large increase, while after the crops started to grow (NDVI and NDWI started to increase), the backscatters and their ratio maintained large values with a slight decrease. During the growing seasons, NDVI and NDWI continued to increase to their maximum values, whereas the backscatters started to decrease before maximum NDVI and NDWI. The relatively high value in backscatters during vegetation growth represented the continuation of the irrigation and the contribution of the vegetation canopy. This observation is consistent with the model simulation. After irrigation was haulted in January 2018 and the vegetation was cleared, the soil moisture approached non-irrigated status and the soil surface was flattened, reducing the surface roughness below that of the natural surface. These changes made the backscatters decrease to values lower than those of the bare ground.

During vegetation growth, the VH-polarized backscatter demonstrated much larger variation in amplitude than the VV-polarized backscatter, and the variation trends of VH and VH/VV were much closer to those of NDVI and NDWI (Figure 6c–e). This observation is consistent with that of the correlation analysis in Section 4.2, demonstrating that VH and VH/VV can reflect the variation of vegetation dynamics. Compared to the planted fields, the backscatter for bare soil demonstrated small values and relatively small variation. The high values over planted fields were caused by vegetation and soil water content.

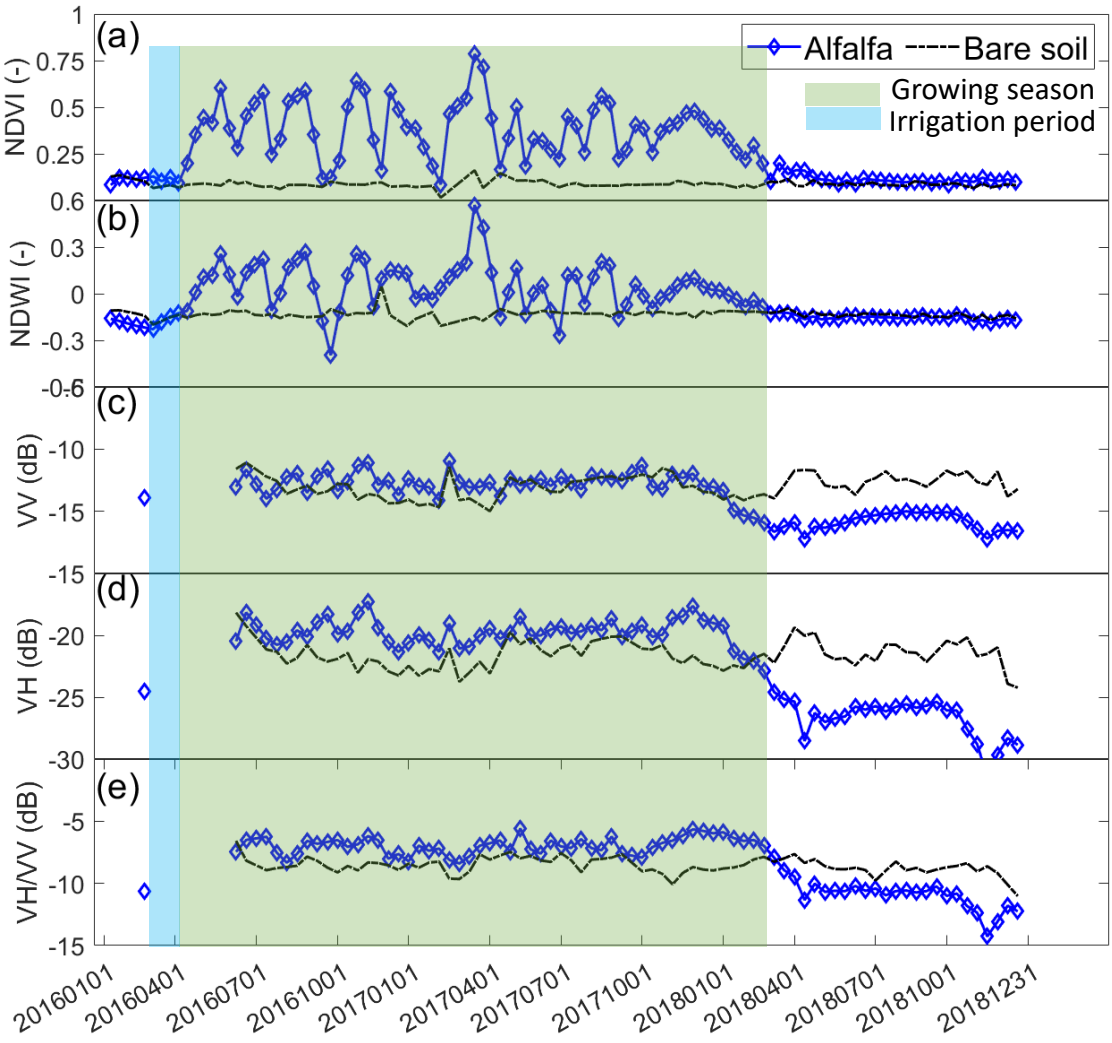

Figure 8. Time series of NDVI (**a**), NDWI (**b**) and backscatters (VV (**c**), VH (**d**) and VH/VV (**e**)) for alfalfa and bare soil from January 2016 to December 2018. The blue bars indicate the beginning of field irrigation in preparation for planting and the green bars indicate the growing seasons of alfalfa (where the irrigation was applied consistently throughout the growing season).

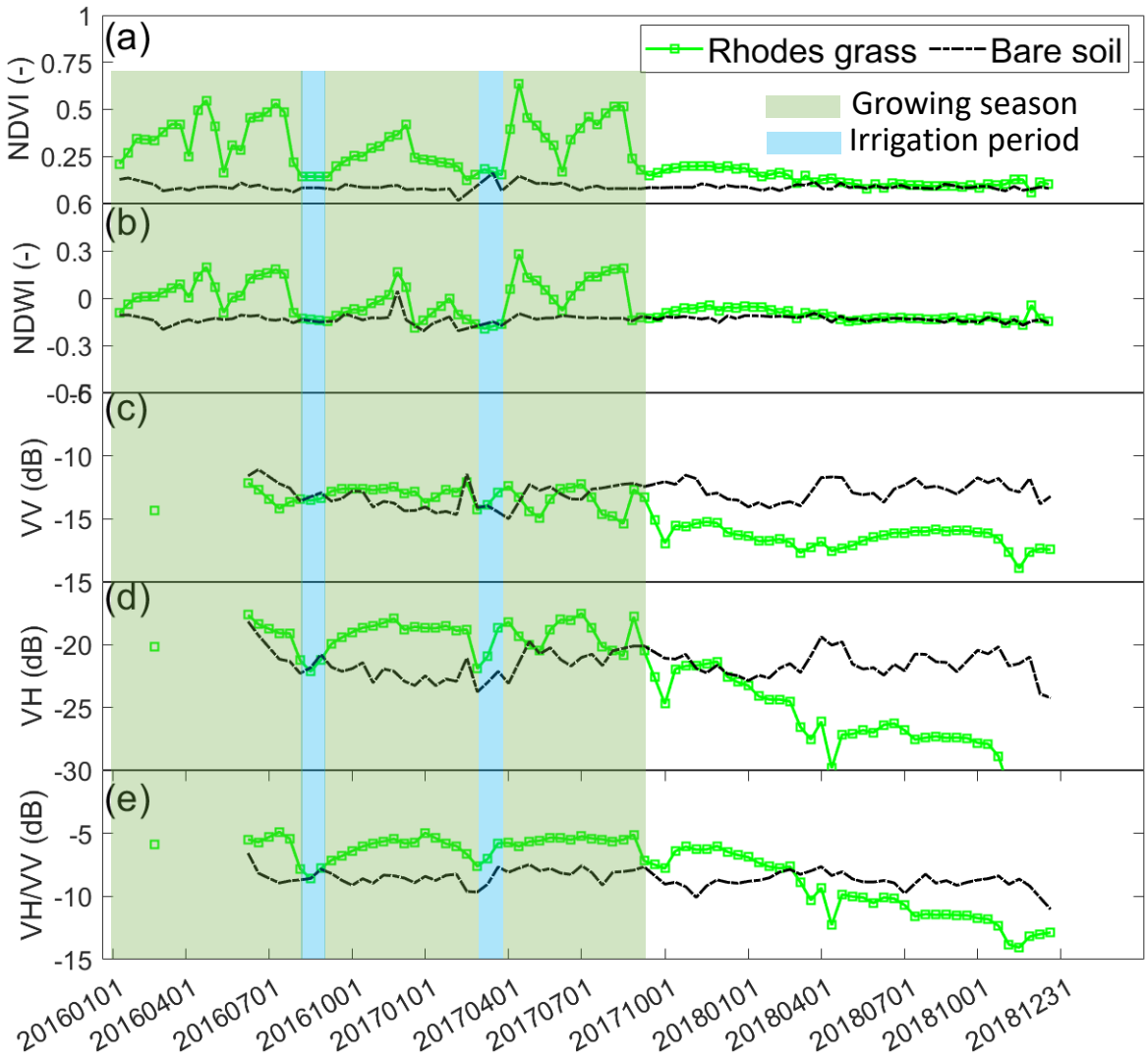

Figure 9. Time series of NDVI (**a**), NDWI (**b**) and backscatters (VV (**c**), VH (**d**) and VH/VV (**e**)) for Rhodes grass and bare soil from January 2016 to December 2018. The blue bars indicate the beginning of field irrigation in preparation for planting and the green bars indicate the growing seasons of Rhodes grass (where the irrigation was applied consistently throughout the growing season).

Similar to what was observed in the maize field, the production routine and growing cycle of carrot (i.e., irrigation applied 15–30 days prior to planting) were well captured by backscatters and both NDVI and NDWI (Figure 7). Carrots were planted from the beginning of 2016 to the end of 2018 in pivot P1-5. However, the length of the growing seasons varied between the different years and were somewhat offset in relation to the growing season for maize. The maximum NDVI and NDWI values were lower than those for maize (Figure 7a,b). Additionally, field P1-5 was continuously planted with carrot in 2018, with individual growing seasons clearly observed in that year.

For the carrot field, VH-polarized backscatter, and the ratio of VH/VV showed inverse variation trends to those of NDVI and NDWI in some growing cycles, including the growing cycle during October 2017 to January 2018. This observation is counter to what was observed in the maize field and might be attributed to the backscatters being more strongly affected by soil surface properties (e.g., surface roughness and soil moisture) than by properties of the vegetation canopy due to the penetration of SAR backscatters within the carrot canopy.

In contrast to the time series of maize and carrot, NDVI, NDWI and backscatters changed frequently for alfalfa Field P22, with no observable seasonal trends due to their rapid growing cycle and the short period between harvest and regrowth (Figure 8). Similarly to the temporal dynamics of NDVI and NDWI, both VV- and VH-polarized backscatters demonstrate highly fluctuating values from June 2016 until January 2018. Much smaller backscatters over the alfalfa field were observed compared to those over bare soil after January 2018, when irrigation was stopped, and the vegetation was cleared.

The NDVI, NDWI and backscatters over Rhodes grass also demonstrated seasonal variation characteristics, but with short growing cycles (Figure 9). A lower frequency was observed in NDVI and NDWI values of Rhodes grass than for that of alfalfa. The P14 field was planted with Rhodes grass from January 2016 until October 2017, with production ceasing in November 2017, causing NDVI and NDWI to approach bare soil values. Both VH-polarized and the VH/VV ratio demonstrated similar variation trends to those of NDVI and NDWI, indicating positive correlation.

Throughout Figures 6, 8 and 9, during both the growing season and irrigated periods, the backscatters over vegetated surfaces were slightly higher than those over bare soil. However, the backscatters over vegetated fields were much smaller than those over bare ground after the end of 2017. This observation provided useful information for discriminating bare soil from previously cultivated soil, where crops had been harvested, cleared or the field had been abandoned.

Statistical measures from the time series of NDVI, NDWI and backscatters were calculated to assess differences between the four types of crops (Table 1). Alfalfa and maize presented the largest maximum values and amplitude in NDVI, followed by Rhodes grass, with the maximum value of carrot being the smallest, likely because of soil exposure in between plants. Based on the statistical measures from the NDVI time series data, carrot and Rhodes grass could be discriminated from alfalfa and maize. While alfalfa and maize appeared with very similar NDVI statistical measures, differences in maximum values and amplitude of NDWI were observed, potentially allowing the two crops to be discriminated. The differences in the length of their growing cycles further aid discrimination.

Table 1. Statistics for NDVI, NDWI and backscatter time series for carrot, Rhodes, alfalfa and maize.

Crops	Statistics	Carrot	Rhodes	Alfalfa	Maize
NDVI	Max	0.48	0.67	0.75	0.75
	Min	0.08	0.04	0.09	0.08
	Amp	0.40	0.63	0.66	0.66
	Std	0.09	0.14	0.17	0.17
NDWI	Max	0.14	0.33	0.56	0.33
	Min	−0.20	−0.19	−0.36	−0.16
	Amp	0.34	0.52	0.92	0.49
	Std	0.08	0.11	0.16	0.13
VV	Max	−8.30	−12.12	−10.95	−8.84
	Min	−16.73	−16.93	−14.20	−18.57
	Amp	8.44	4.80	3.19	9.73
	Std	1.88	1.01	0.76	1.96
VH	Max	−17.22	−17.50	−17.28	−16.66
	Min	−26.14	−24.71	−24.53	−27.83
	Amp	8.92	7.22	7.26	11.16
	Std	2.81	1.50	1.14	3.21
VH/VV	Max	−5.83	−4.89	−5.58	−5.54
	Min	−13.72	−8.60	−10.66	−12.28
	Amp	7.89	3.70	5.08	6.74
	Std	1.84	0.90	0.84	2.20

There are limited differences in maximum and minimum values of the backscatters for the different crops, but differences can be observed in their amplitude and standard deviations [11–13]. For example, the amplitude and standard deviation of VV-polarized

backscatters for maize and carrot were twice as high as those for Rhodes and alfalfa, demonstrating that the backscatters of the maize and carrot fields had larger dynamics than those of the Rhodes and alfalfa fields. Thus, the differences among these statistical features could be potentially applied to the classification of crops.

5. Discussion

Here, we explore a time series of Sentinel-1 and Sentinel-2 data for monitoring agronomic events and crop growth dynamics over a three-year period to gain a better understanding of the interaction between SAR backscatter and surface processes of agricultural fields. Below we discuss key findings and their potential application.

5.1. Estimating VWC and Monitoring Crop Dynamics with Combined Sentinel-1/2 Data

The correlation analysis between SAR backscatters and both NDVI and NDWI demonstrated that the VH/VV ratio and VH-polarized backscatter had relatively high correlation with the optical indices (NDVI, NDWI), indicating that the VH/VV ratio and VH-polarized backscatter can potentially be used for VWC estimation, as NDVI and NDWI have previously been proven to be able to estimate VWC [6] and monitor the crop dynamics [11–13]. Exploiting this potential may provide an alternative when the NDVI and NDWI are not available under either cloudy or rainy conditions.

SAR-based VWC has gained considerable research interest in recent years [54,55], with the exploration of the radar vegetation index (RVI) [56,57] as a proxy to estimate VWC. Several recent studies have found that cross-polarized backscatters and the ratio of VH/VV also correlate well with VWC. For example, Twele [58] found that HV-polarized backscatter provided an improved estimate of VWC when compared to the RVI. In another example, Veloso et al. [37] found that the ratio of VH/VV reproduced similar temporal trends to the NDVI and can be potentially applied for VWC estimation and monitoring. Vreugdenhil et al. [59] demonstrated that VH/VV could account for 87% and 63% of the variability in VWC for corn and winter cereals. The estimation of VWC from NDVI and NDWI has been extensively reported, particularly in the work of Jackson et al. [10], Chen et al. [9] and Gao et al. [6]. Our analysis indicates a high correlation between VH/VV and NDVI/NDWI, which is consistent with the findings of Veloso et al. [37], further supporting the application of Sentinel-1 SAR for VWC estimation.

Through the combination of high spatio-temporal resolution SAR and optical image data, vegetation dynamics can be identified. Some previous research investigated the synergy of optical and SAR data for crop inventories [60] and identification [61], demonstrating high feasibility of monitoring crop dynamics using combined SAR and optical images. Our research presented herein further demonstrates this feasibility by introducing higher spatio-temporal resolution images compared to previous studies [60,61]. Denser time-series provide more detailed information about the agricultural status and processes and reduce limitations of cloud issues. In addition to identifying key crop phenological stages, such as germination/planting and crop maturity/harvesting dates, the combined SAR-optical data can quantitatively estimate vegetation water content and other variables [62], as well as map land cover [63], which would advance applications combining multi-source high-resolution remote sensing data for precision agriculture.

5.2. Combining Sentinel-1 and Sentinel-2 for Identifying Irrigation Events

SAR images have previously been found to be suitable for monitoring irrigation due to the high sensitivity of SAR backscatters to soil moisture [64–69]. However, the use of SAR data for mapping agricultural irrigation only became practical after the launch of the Sentinel-1 mission, due to its high spatial and temporal resolution, enabling dense time series of SAR observations to be consistently obtained. Based on forward modeling and correlation analysis, our results not only support previous findings in Gao [70] and Bazzi [71], where Sentinel-1 was used for irrigation mapping using statistical analysis and machine learning, but also quantify the influence of irrigation on the backscatters. Both

model simulation (Figure 2) and time series analysis (Figures 4 and 6–9) demonstrated that Sentinel-1 data could capture the start and end points of irrigation due to distinct temporal changes in soil moisture.

The combination of Sentinel-1 SAR and Senitnel-2 optical images can enhance the identification of irrigation events. On the one hand, both Sentinel-1 and 2 data have high spatial resolution and short revisit cycles, making their dual-use well suited to capture within field scale agronomic events and crop dynamics. On the other hand, Sentinel-1 SAR backscatters are sensitive to variability in soil wetness, while the Sentinel-2-derived NDVI and NDWI can track the crop growth process. In arid regions, irrigation usually starts prior to planting and after several weeks, the plant starts to grow. Thus, if an increase in SAR backscatters is followed by an increase in Sentinel-2-derived NDVI (or NDWI), it is likely that the increase in backscatter is caused by irrigation and the increase in NDVI and NDWI is caused by plant growth. This combined information (the backscattering and NDVI/NDWI increase successively) reflects the beginning of the irrigation events and crop growth.

Here, we have demonstrated that it is feasible to identify the irrigation events and start point of crop growth by combining Sentinel-1 and 2 images. Here, we provide a qualitative analysis of such feasibility and potential. Prospectively, the value of such information may best be realized through combination with other quantitative estimates of field-based agroinformatics. For example, improved estimation of irrigated water volumes is of considerable interest for precision irrigation and water resources management, and these could benefit from more precise monitoring of irrigation start and end points (particularly in pre-planting irrigation). Indeed, efforts and progress have been made towards this direction, such as the work by Aragon et al. [72] and Johansen et al. [73] based on CubeSat image time-series; thus, combining qualitative and quantitative measures will help deliver further precision agricultural insights.

Another aspect that requires further consideration is that the present study was undertaken in an ideal research setting, where Sentinel-2 optical images were rarely constrained by cloud, ensuring collections of dense time series of optical images. If the methods used here were applied in other locations (i.e., where optical imagery were more frequently affected by clouds), overcoming the shortage of optical data may present as a significant challenge. However, the increased resolution and frequency of CubeSat-based platforms might provide a means of accounting for such temporal gaps [72,73]. In addition, using temporal interpolation methods based on multi-platform optical images to fill the gaps in the optical image time series can be a potential solution [33]. Furthermore, available optical-SAR image pairs may be used to train a machine learning based relation between SAR and optical images, with such relation potentially being used to restore the optical image time series based on SAR data to reduce the effects of poor weather conditions [74].

6. Conclusions

A combination of Sentinel-1 and Sentinel-2 time series data were used to monitor irrigation events and dynamics over four different crop types across a 3-year period. The time series analysis was performed based on forward model simulation and correlation analysis, as well as via verification from field-based farming records. The forward modeling established the links between SAR backscatters and optical NDVI and NDWI indices, and revealed the relation of backscatters to soil moisture, NDVI and NDWI, providing a theoretical foundation for the time series analysis. The correlation analysis demonstrated that SAR backscatters at both polarizations together with their ratio were well correlated with observed variations in NDVI and NDWI. These observations demonstrated the feasibility and reliability of monitoring irrigation events and vegetation dynamics using a combination of Sentinel-1 and Sentinel-2 data. Our research also demonstrates the possibility of using the VH/VV ratio and VH-polarized backscatter as an alternative for describing vegetation under cloudy conditions when optical images may not be available. Overall, the present study demonstrates the complementarity of Sentinel-1 and Sentinel-2 satellite data

to identify irrigation events and monitor crop dynamics for precision agriculture. Further quantitative evaluation of agricultural production events and retrievable variables (such as irrigation volume) across a range of different landscape and climate settings is required to explore the broad-scale application of this approach.

Author Contributions: M.F.M. and C.M. conceived the project. C.M. analyzed the data and compiled the results. C.M. wrote the manuscript with the guidance of M.F.M. and K.J. All authors discussed the results and contributed to the writing and editing of the manuscript. All authors have read and agreed to the published version of the manuscript.

Funding: The research reported in this publication was supported by the King Abdullah University of Science and Technology (KAUST), Saudi Arabia.

Institutional Review Board Statement: Not applicable.

Informed Consent Statement: Not applicable.

Data Availability Statement: Data presented in this study are available upon request from the corresponding author.

Acknowledgments: Sentinel-1 and Sentinel-2 images were obtained from ESA, and the agricultural records were provided by the Al Kharj Farm in Al Kharj, Saudi Arabia. The authors would like to thank all the above-mentioned institutions and individuals for their help and support.

Conflicts of Interest: The authors declare no conflict of interest.

References

1. Hussain, Z. Problems of Irrigated Agriculture in Al-Hassa, Saudi-Arabia. *Agric. Water Manag.* **1982**, *5*, 359–374. [CrossRef]
2. Hussain, G.; Al-Saati, A.J. Wastewater quality and its reuse in agriculture in Saudi Arabia. *Desalination* **1999**, *123*, 241–251. [CrossRef]
3. Qin, W.; Wang, D.Z.; Guo, X.S.; Yang, T.M.; Oenema, O. Productivity and sustainability of rainfed wheat-soybean system in the North China Plain: Results from a long-term experiment and crop modelling. *Sci. Rep.* **2015**, *5*, 17514. [CrossRef]
4. Ezenne, G.I.; Jupp, L.; Mantel, S.K.; Tanner, J.L. Current and potential capabilities of UAS for crop water productivity in precision agriculture. *Agric. Water Manag.* **2019**, *218*, 158–164. [CrossRef]
5. Zewdie, W.; Csaplovics, E.; Inostroza, L. Monitoring ecosystem dynamics in northwestern Ethiopia using NDVI and climate variables to assess long term trends in dryland vegetation variability. *Appl. Geogr.* **2017**, *79*, 167–178. [CrossRef]
6. Gao, Y.; Walker, J.P.; Allahmoradi, M.; Monerris, A.; Ryu, D.; Jackson, T.J. Optical Sensing of Vegetation Water Content: A Synthesis Study. *IEEE J. Sel. Top. Appl. Earth Obs. Remote Sens.* **2015**, *8*, 1456–1464. [CrossRef]
7. Jonsson, P.; Cai, Z.Z.; Melaas, E.; Friedl, M.A.; Eklundh, L. A Method for Robust Estimation of Vegetation Seasonality from Landsat and Sentinel-2 Time Series Data. *Remote Sens.* **2018**, *10*, 635. [CrossRef]
8. Verbesselt, J.; Somers, B.; van Aardt, J.; Jonckheere, I.; Coppin, P. Monitoning herbaceous biomass and water content with SPOT VEGETATION time-series to improve fire risk assessment in savanna ecosystems. *Remote Sens. Environ.* **2006**, *101*, 399–414. [CrossRef]
9. Chen, D.; Huang, J.; Jackson, T.J. Vegetation water content estimation for corn and soybeans using spectral indices derived from MODIS near- and short-wave infrared bands. *Remote Sens. Environ.* **2005**, *98*, 225–236. [CrossRef]
10. Jackson, T.J.; Chen, D.Y.; Cosh, M.; Li, F.Q.; Anderson, M.; Walthall, C.; Doriaswamy, P.; Hunt, E.R. Vegetation water content mapping using Landsat data derived normalized difference water index for corn and soybeans. *Remote Sens. Environ.* **2004**, *92*, 475–482. [CrossRef]
11. Sakamoto, T.; Yokozawa, M.; Toritani, H.; Shibayama, M.; Ishitsuka, N.; Ohno, H. A crop phenology detection method using time-series MODIS data. *Remote Sens. Environ.* **2005**, *96*, 366–374. [CrossRef]
12. Sisheber, B.; Marshall, M.; Mengistu, D.; Nelson, A. Tracking crop phenology in a highly dynamic landscape with knowledge-based Landsat–MODIS data fusion. *Int. J. Appl. Earth Obs. Geoinf.* **2022**, *106*, 102670. [CrossRef]
13. Cavaliere, D.; Senatore, S. Incremental Knowledge Extraction from IoT-Based System for Anomaly Detection in Vegetation Crops. *IEEE J. Sel. Top. Appl. Earth Obs. Remote Sens.* **2022**, *15*, 876–888. [CrossRef]
14. Pan, L.; Xia, H.; Yang, J.; Niu, W.; Wang, R.; Song, H.; Guo, Y.; Qin, Y. Mapping cropping intensity in Huaihe basin using phenology algorithm, all Sentinel-2 and Landsat images in Google Earth Engine. *Int. J. Appl. Earth Obs. Geoinf.* **2021**, *102*, 102376. [CrossRef]
15. Gupta, D.K.; Prasad, R.; Kumar, P.; Vishwakarma, A.K.; Srivastava, P.K. Vegetation water content retrieval using scatterometer data at X-band. *Geocarto Int.* **2018**, *33*, 602–611. [CrossRef]
16. Li, J.H.; Wang, S.S. Using SAR-Derived Vegetation Descriptors in a Water Cloud Model to Improve Soil Moisture Retrieval. *Remote Sens.* **2018**, *10*, 1370. [CrossRef]

17. Ma, C.; Li, X.; Chen, K.S. The Discrepancy between Backscattering Model Simulations and Radar Observations Caused by Scaling Issues: An Uncertainty Analysis. *IEEE Trans. Geosci. Remote Sens.* **2019**, *57*, 5356–5372. [CrossRef]
18. Ma, X.S.; Wu, P.H.; Shen, H.F. A Nonlinear Guided Filter for Polarimetric SAR Image Despeckling. *IEEE Trans. Geosci. Remote Sens.* **2019**, *57*, 1918–1927. [CrossRef]
19. McCabe, M.; Aragon, B.; Houborg, R.; Mascaro, J. CubeSats in hydrology: Ultrahigh-resolution insights into vegetation dynamics and terrestrial evaporation. *Water Resour. Res.* **2017**, *53*, 10017–10024. [CrossRef]
20. Malenovský, Z.; Rott, H.; Cihlar, J.; Schaepman, M.E.; García-Santos, G.; Fernandes, R.; Berger, M. Sentinels for science: Potential of Sentinel-1, -2, and -3 missions for scientific observations of ocean, cryosphere, and land. *Remote Sens. Environ.* **2012**, *120*, 91–101. [CrossRef]
21. Hornacek, M.; Wagner, W.; Sabel, D.; Truong, H.-L.; Snoeij, P.; Hahmann, T.; Diedrich, E.; Doubkova, M. Potential for High Resolution Systematic Global Surface Soil Moisture Retrieval via Change Detection Using Sentinel-1. *IEEE J. Sel. Top. Appl. Earth Obs. Remote Sens.* **2012**, *5*, 1303–1311. [CrossRef]
22. Paloscia, S.; Pettinato, S.; Santi, E.; Notarnicola, C.; Pasolli, L.; Reppucci, A. Soil moisture mapping using Sentinel-1 images: Algorithm and preliminary validation. *Remote Sens. Environ.* **2013**, *134*, 234–248. [CrossRef]
23. Sabel, D.; Bartalis, Z.; Wagner, W.; Doubkova, M.; Klein, J.-P. Development of a Global Backscatter Model in support to the Sentinel-1 mission design. *Remote Sens. Environ.* **2012**, *120*, 102–112. [CrossRef]
24. Drusch, M.; Del Bello, U.; Carlier, S.; Colin, O.; Fernandez, V.; Gascon, F.; Hoersch, B.; Isola, C.; Laberinti, P.; Martimort, P.; et al. Sentinel-2: ESA's Optical High-Resolution Mission for GMES Operational Services. *Remote Sens. Environ.* **2012**, *120*, 25–36. [CrossRef]
25. Vanino, S.; Nino, P.; De Michele, C.; Bolognesi, S.F.; D'Urso, G.; Di Bene, C.; Pennelli, B.; Vuolo, F.; Farina, R.; Pulighe, G.; et al. Capability of Sentinel-2 data for estimating maximum evapotranspiration and irrigation requirements for tomato crop in Central Italy. *Remote Sens. Environ.* **2018**, *215*, 452–470. [CrossRef]
26. Pierdicca, N.; Pulvirenti, L.; Pace, G. A Prototype Software Package to Retrieve Soil Moisture from Sentinel-1 Data by Using a Bayesian Multitemporal Algorithm. *IEEE J. Sel. Top. Appl. Earth Obs. Remote Sens.* **2014**, *7*, 153–166. [CrossRef]
27. Bauer-Marschallinger, B.; Freeman, V.; Cao, S.; Paulik, C.; Schaufler, S.; Stachl, T.; Modanesi, S.; Massari, C.; Ciabatta, L.; Brocca, L.; et al. Toward Global Soil Moisture Monitoring with Sentinel-1: Harnessing Assets and Overcoming Obstacles. *IEEE Trans. Geosci. Remote Sens.* **2018**, *57*, 520–539. [CrossRef]
28. El Hajj, M.; Baghdadi, N.; Zribi, M.; Bazzi, H. Synergic Use of Sentinel-1 and Sentinel-2 Images for Operational Soil Moisture Mapping at High Spatial Resolution over Agricultural Areas. *Remote Sens.* **2017**, *9*, 1292. [CrossRef]
29. Ma, C.; Li, X.; McCabe, M.F. Retrieval of High-Resolution Soil Moisture through Combination of Sentinel-1 and Sentinel-2 Data. *Remote Sens.* **2020**, *12*, 2303. [CrossRef]
30. Kolecka, N.; Ginzler, C.; Pazur, R.; Price, B.; Verburg, P.H. Regional Scale Mapping of Grassland Mowing Frequency with Sentinel-2 Time Series. *Remote Sens.* **2018**, *10*, 1221. [CrossRef]
31. Belgiu, M.; Csillik, O. Sentinel-2 cropland mapping using pixel-based and object-based time-weighted dynamic time warping analysis. *Remote Sens. Environ.* **2018**, *204*, 509–523. [CrossRef]
32. Vrieling, A.; Meroni, M.; Darvishzadeh, R.; Skidmore, A.K.; Wang, T.J.; Zurita-Milla, R.; Oosterbeek, K.; O'Connor, B.; Paganini, M. Vegetation phenology from Sentinel-2 and field cameras for a Dutch barrier island. *Remote Sens. Environ.* **2018**, *215*, 517–529. [CrossRef]
33. Pan, L.; Xia, H.; Zhao, X.; Guo, Y.; Qin, Y. Mapping Winter Crops Using a Phenology Algorithm, Time-Series Sentinel-2 and Landsat-7/8 Images, and Google Earth Engine. *Remote Sens.* **2021**, *13*, 2510. [CrossRef]
34. Sun, L.Y.; Chen, J.S.; Guo, S.X.; Deng, X.P.; Han, Y. Integration of Time Series Sentinel-1 and Sentinel-2 Imagery for Crop Type Mapping over Oasis Agricultural Areas. *Remote Sens.* **2020**, *12*, 158. [CrossRef]
35. Van Tricht, K.; Gobin, A.; Gilliams, S.; Piccard, I. Synergistic Use of Radar Sentinel-1 and Optical Sentinel-2 Imagery for Crop Mapping: A Case Study for Belgium. *Remote Sens.* **2018**, *10*, 1642. [CrossRef]
36. Orynbaikyzy, A.; Gessner, U.; Mack, B.; Conrad, C. Crop Type Classification Using Fusion of Sentinel-1 and Sentinel-2 Data: Assessing the Impact of Feature Selection, Optical Data Availability, and Parcel Sizes on the Accuracies. *Remote Sens.* **2020**, *12*, 2779. [CrossRef]
37. Veloso, A.; Mermoz, S.; Bouvet, A.; Le Toan, T.; Planells, M.; Dejoux, J.-F.; Ceschia, E. Understanding the temporal behavior of crops using Sentinel-1 and Sentinel-2-like data for agricultural applications. *Remote Sens. Environ.* **2017**, *199*, 415–426. [CrossRef]
38. Capodici, F.; D'Urso, G.; Maltese, A. Investigating the relationship between X-Band SAR Data from COSMO-SkyMed Satellite and NDVI for LAI detection. *Remote Sens.* **2013**, *5*, 1389–1404. [CrossRef]
39. Bai, Z.; Fang, S.; Gao, J.; Zhang, Y.; Jin, G.; Wang, S.; Zhu, Y.; Xu, J. Could Vegetation index be Derive from Synthetic Aperture Radar?–the Linear Relationship between interferometric coherence and nDVi. *Sci. Rep.* **2020**, *10*, 6749. [CrossRef]
40. Alkolibi, F.M. Possible Effects of Global Warming on Agriculture and Water Resources in Saudi Arabia: Impacts and Responses. *Clim. Chang.* **2002**, *54*, 225–245. [CrossRef]
41. Houborg, R.; McCabe, M.F. A hybrid training approach for leaf area index estimation via Cubist and random forests machine-learning. *ISPRS J. Photogramm. Remote Sens.* **2018**, *135*, 173–188. [CrossRef]
42. Houborg, R.; McCabe, M.F. A Cubesat enabled Spatio-Temporal Enhancement Method (CESTEM) utilizing Planet, Landsat and MODIS data. *Remote Sens. Environ.* **2018**, *209*, 211–226. [CrossRef]

43. Torres, R.; Snoeij, P.; Geudtner, D.; Bibby, D.; Davidson, M.; Attema, E.; Potin, P.; Rommen, B.; Floury, N.; Brown, M.; et al. GMES Sentinel-1 mission. *Remote Sens. Environ.* **2012**, *120*, 9–24. [CrossRef]
44. Gorelick, N.; Hancher, M.; Dixon, M.; Ilyushchenko, S.; Thau, D.; Moore, R. Google Earth Engine: Planetary-scale geospatial analysis for everyone. *Remote Sens. Environ.* **2017**, *202*, 18–27. [CrossRef]
45. Gascon, F.; Ramoino, F. Sentinel-2 data exploitation with ESA's Sentinel-2 Toolbox. *EGU Gen. Assem. Conf. Abstr.* **2017**, *19*, 19548.
46. Mandal, D.; Kumare, V.; Bhattacharya, A.; Rao, Y.S.; Siqueira, P.; Bera, S. Sen4Rice: A Processing Chain for Differentiating Early and Late Transplanted Rice Using Time-Series Sentinel-1 SAR Data With Google Earth Engine. *IEEE Geosci. Remote Sens. Lett.* **2018**, *15*, 1947–1951. [CrossRef]
47. Louis, J.; Debaecker, V.; Pflug, B.; Main-Knorn, M.; Bieniarz, J.; Mueller-Wilm, U.; Cadau, E.; Gascon, F. Sentinel-2 Sen2Cor: L2A Processor for Users. In Proceedings of the Living Planet Symposium 2016, Prague, Czech Republic, 9–13 May 2016; pp. 1–8.
48. Chen, D.Y.; Jackson, T.J.; Li, F.; Cosh, M.H.; Walthall, C.; Anderson, M. Estimation of vegetation water content for corn and Soybeans with a Normalized Difference Water Index (NDWI) using Landsat Thematic Mapper data. In Proceedings of the 2003 IEEE International Geoscience and Remote Sensing Symposium, Toulouse, France, 21–25 July 2003; pp. 2853–2856.
49. Attema, E.P.W.; Ulaby, F.T. Vegetation Modeled as a Water Cloud. *Radio Sci.* **1978**, *13*, 357–364. [CrossRef]
50. Bindlish, R.; Barros, A.P. Parameterization of vegetation backscatter in radar-based, soil moisture estimation. *Remote Sens. Environ.* **2001**, *76*, 130–137. [CrossRef]
51. Oh, Y. Quantitative Retrieval of Soil Moisture Content and Surface Roughness From Multipolarized Radar Observations of Bare Soil Surfaces. *IEEE Trans. Geosci. Remote Sens.* **2004**, *42*, 596–601. [CrossRef]
52. Fung, A.K.; Li, Z.Q.; Chen, K.S. Backscattering from a Randomly Rough Dielectric Surface. *IEEE Trans. Geosci. Remote Sens.* **1992**, *30*, 356–369. [CrossRef]
53. Hornbuckle, B.; Walker, V.; Eichinger, B.; Wallace, V.; Yildirim, E. Soil surface roughness observed during SMAPVEX16-IA and its potential consequences for SMOS and SMAP. *IEEE Int. Geosci. Remote Sens. Symp.* **2017**, *2017*, 2027–2030.
54. Notarnicola, C.; Posa, F. Inferring vegetation water content from C- and L-band SAR images. *IEEE Trans. Geosci. Remote Sens.* **2007**, *45*, 3165–3171. [CrossRef]
55. Pulliainen, J.; Hari, P.; Hallikainen, M.; Patrikainen, N.; Peramaki, M.; Kolari, P. Monitoring of soil moisture and vegetation water content variations in boreal forest from C-band SAR data. *IEEE Int. Geosci. Remote Sens. Symp.* **2004**, *2*, 1013–1016.
56. Kim, Y.; Jackson, T.; Bindlish, R.; Lee, H.; Hong, S. Radar Vegetation Index for Estimating the Vegetation Water Content of Rice and Soybean. *IEEE Geosci. Remote Sens. Lett.* **2012**, *9*, 564–568.
57. Huang, Y.C.; Walker, J.P.; Gao, Y.; Wu, X.L.; Monerris, A. Estimation of Vegetation Water Content From the Radar Vegetation Index at L-Band. *IEEE Trans. Geosci. Remote Sens.* **2016**, *54*, 981–989. [CrossRef]
58. Twele, A. Sentinel-1-based flood mapping: A fully automated processing chain. *Int. J. Remote Sens.* **2016**, *37*, 2990–3004. [CrossRef]
59. Vreugdenhil, M.; Wagner, W.; Bauer-Marschallinger, B.; Pfeil, I.; Teubner, I.; Rüdiger, C.; Strauss, P. Sensitivity of Sentinel-1 backscatter to vegetation dynamics: An Austrian case study. *Remote Sens.* **2018**, *10*, 1396. [CrossRef]
60. McNairn, H.; Champagne, C.; Shang, J.; Holmstrom, D.; Reichert, G. Integration of optical and Synthetic Aperture Radar (SAR) imagery for delivering operational annual crop inventories. *ISPRS J. Photogramm. Remote Sens.* **2009**, *64*, 434–449. [CrossRef]
61. Blaes, X.; Vanhalle, L.; Defourny, P. Efficiency of crop identification based on optical and SAR image time series. *Remote Sens. Environ.* **2005**, *96*, 352–365. [CrossRef]
62. Irwin, K.; Beaulne, D.; Braun, A.; Fotopoulos, G. Fusion of SAR, Optical Imagery and Airborne LiDAR for Surface Water Detection. *Remote Sens.* **2017**, *9*, 890. [CrossRef]
63. Vaglio Laurin, G.; Liesenberg, V.; Chen, Q.; Guerriero, L.; Del Frate, F.; Bartolini, A.; Coomes, D.; Wilebore, B.; Lindsell, J.; Valentini, R. Optical and SAR sensor synergies for forest and land cover mapping in a tropical site in West Africa. *Int. J. Appl. Earth Obs. Geoinf.* **2013**, *21*, 7–16. [CrossRef]
64. Weimann, A.; Von Schonermark, M.; Schumann, A.; Jorn, P.; Gunther, R. Soil moisture estimation with ERS-1 SAR data in the East-German loess soil area. *Int. J. Remote Sens.* **1998**, *19*, 237–243. [CrossRef]
65. Biftu, G.F.; Gan, T.Y. Retrieving near-surface soil moisture from Radarsat SAR data. *Water Resour. Res.* **1999**, *35*, 1569–1579. [CrossRef]
66. Saradjian, M.R.; Hosseini, M. Soil moisture estimation by using multipolarization SAR image. *Adv. Space Res.* **2011**, *48*, 278–286. [CrossRef]
67. Zribi, M.; Kotti, F.; Amri, R.; Wagner, W.; Shabou, M.; Lili-Chabaane, Z.; Baghdadi, N. Soil moisture mapping in a semiarid region, based on ASAR/Wide Swath satellite data. *Water Resour. Res.* **2014**, *50*, 823–835. [CrossRef]
68. Ma, C.; Li, X.; Wang, S. A Global Sensitivity Analysis of Soil Parameters Associated with Backscattering Using the Advanced Integral Equation Model. *IEEE Trans. Geosci. Remote Sens.* **2015**, *53*, 5613–5623.
69. Ma, C.; Wang, S.; Zhao, Z.; Ma, H. Global Sensitivity Analysis of a Water Cloud Model toward Soil Moisture Retrieval over Vegetated Agricultural Fields. *Remote Sens.* **2021**, *13*, 3889. [CrossRef]
70. Gao, Q. Irrigation mapping using Sentinel-1 time series at field scale. *Remote Sens.* **2018**, *10*, 1495. [CrossRef]
71. Bazzi, H.; Baghdadi, N.; Ienco, D.; El Hajj, M.; Zribi, M.; Belhouchette, H.; Escorihuela, M.J.; Demarez, V. Mapping irrigated areas using Sentinel-1 Time series in Catalonia, Spain. *Remote Sens.* **2019**, *11*, 1836. [CrossRef]
72. Aragon, B.; Ziliani, M.G.; Houborg, R.; Franz, T.E.; McCabe, M.F. CubeSats deliver new insights into agricultural water use at daily and 3 m resolutions. *Sci. Rep.* **2021**, *11*, 12131. [CrossRef]

73. Johansen, K.; Ziliani, M.G.; Houborg, R.; Franz, T.E.; McCabe, M.F. Cubesat Constellations Provide Enhanced Crop Phenology And Digital Agricultural Insights Using Daily Leaf Area Index Retrievals. *Sci. Rep.* **2022**, 1–16. [CrossRef]
74. Sebastianelli, A.; Nowakowski, A.; Puglisi, E.; Rosso, M.P.d.; Mifdal, J.; Pirri, F.; Mathieu, P.-P.; Ullo, S.L. Spatio-Temporal SAR-Optical Data Fusion for Cloud Removal via a Deep Hierarchical Model. *arXiv* **2021**, arXiv:2106.12226.